High thermal conductivity in isotopically enriched cubic boron phosphide

Qiye Zheng, Sheng Li, Chunhua Li, Yinchuan Lv, Xiaoyuan Liu, Pinshane Y. Huang, David A. Broido, Bing Lv, and David G. Cahill**

Dr. Qiye Zheng, Prof. Pinshane Y. Huang, and Prof. David G. Cahill
Department of Materials Science and Engineering,
Materials Research Laboratory, University of Illinois at Urbana-Champaign, Urbana, Illinois 61801, USA
E-mail: d-cahill@illinois.edu
Yinchuan Lv
Department of Physics,
University of Illinois at Urbana-Champaign,
Urbana, Illinois 61801, USA
Dr. Sheng Li, Xiaoyuan Liu, and Prof. Bing Lv
E-mail: blv@utdallas.edu
Department of Physics, The University of Texas at Dallas, Richardson, TX 75080 USA
Dr. Chunhua Li, Prof. David A. Broido
Department of Physics, Boston College, Chestnut Hill, Massachusetts 02467, USA

Keywords: high thermal conductivity material, isotope enrichment effect, time-domain thermoreflectance, first principles calculation, Raman spectroscopy

Abstract

Zinc blende BAs, BP, and BN have attracted significant interest in recent years due to their high thermal conductivity (Λ) predicted by first principles calculations. Here, we report our study of the temperature dependence of Λ (120 K < T < 600 K) for natural isotope-abundance BP and isotopically-enriched ^{11}BP crystals grown from modified flux reactions. We use time-domain thermoreflectance to measure Λ of sub-mm sized crystals. At room temperature, Λ for BP and ^{11}BP are 490 and 540 W m^{-1} K^{-1}, respectively, surpassing the values of conventional high Λ materials such as Ag, Cu, BeO, and SiC. The Λ of BP is smaller than only c-BN, diamond, graphite and BAs among single-phase materials. The measured Λ for BP and ^{11}BP are in good agreement with our first principles calculations above 250 K. The quality of the crystals is verified by Raman spectroscopy, X-ray diffraction, and scanning transmission electron microscopy. By combining first principles calculations and Raman measurements, we reassign a previously misinterpreted Raman mode. BP thus is a promising material not only for heat

spreader applications in high-power microelectronic devices but also as an electronic material for use in harsh environments.

Recent advances in device miniaturization have led to highly nonuniform power distribution in microelectronic devices, producing "hot spots" with heat fluxes on the order of 1 kW cm^{-2}.[1, 2] Thermal management of concentrated heat sources is a critical bottleneck for a broad range of applications: microprocessors, smart phones, telecommunication systems and data centers.[2, 3] Although strategies such as power optimization design,[4, 5] and localized cooling with microfluid channels or thermoelectrics have been developed,[5] mitigating the temperature excursion of "hot spots" remains challenging.[5] The intrinsic thermal conductivity Λ of diamond is exceptionally high, $\approx$ 2200 W m^{-1} K^{-1} at room temperature, and it is sometimes used as a heat spreader in electronics. Bulk diamond composites fabricated by sintering of microcrystalline diamond with a binder metal or by metal infiltration (with typical thermal conductivity of a few hundred W m^{-1} K^{-1}) are often used as a board-level heat sink.[6] However, direct production of wafer-scale CVD diamond for chip-level heat dissipation is still expensive. For example, a 30 mm diameter 500 μm thick diamond film with thermal conductivity of 900 to 1000 W m^{-1} K^{-1} costs >$4500 (by Applied Diamond Inc.).

Recent *ab initio* calculations predict ultrahigh room temperature thermal conductivities Λ in several cubic III-V boron compounds. The highest predicted value at 300 K, 2200 W m^{-1} K^{-1} for boron arsenide (BAs), is based on the assumption that phonon lifetimes are dominated by three-phonon scattering.[7] A recent extension of the theory to include four-phonon processes predicts 1400 W m^{-1} K^{-1} at room temperature.[8] The initial measurements of Λ in BAs showed relatively small values from 200 to 350 W m^{-1} K^{-1} ; very recently, Λ of 1000 to 1300 W m^{-1} K^{-1} were obtained in BAs crystals with limited yield of samples with high thermal conductivity.[9] For BAs samples with relatively low Λ, phonon lifetimes are presumably limited by residual defects and impurities.[10] Cubic boron nitride (c-BN) is also predicted to have high Λ of 940

W m^{-1} K^{-1}. Experiments on c-BN have observed 740 W m^{-1} K^{-1} at room temperature.[7, 11] However, c-BN is difficult to synthesize, typically requiring high temperatures (>2000 °C) and pressures (10 GPa). As far as we know, there is no commercial heat spreader made of c-BN that is currently available in the market although we note that h-BN powder with thermal conductivity <200 W m^{-1} K^{-1} is sometimes used as a filler in thermally conductive composites.

The thermal conductivity Λ of boron phosphide (BP) was also predicted to be exceptionally high, Λ = 580 W m^{-1} K^{-1}.[7] Prior experiments on the room temperature thermal conductivity of BP with natural isotopic abundance (19.9 wt. % of ^{10}B and 80.1 wt. % of ^{11}B; P is naturally isotopically pure) range from 360 to 460 W m^{-1} K^{-1},[12-14] close to the results of first principles calculations.[7] Further enhancement of Λ in BP should be possible through isotope enrichment of boron and improvement in crystal quality.[15]

In addition to high Λ, BP also has other outstanding properties such as chemical inertness,[16] stability at high temperatures,[16] and high mechanical hardness.[17] BP is extremely hard, with a bulk modulus of 172 GPa and a Vickers microhardness (39 GPa) twice that of sapphire, 30% greater SiC, and a factor of 2.5 smaller than the hardness of diamond, ≈100 GPa.[17] The high hardness of BP should not limit the application of BP as thick film heat spreader since processing techniques such as diamond saw or laser cutting, mechanical and chemical-mechanical polishing that are routinely used in SiC film fabrication may also be applied to BP. [18] BP has a relatively low density of 2.9 g cm^{-3} which is slightly higher than Al (2.7 g cm^{-3}) and slightly less than SiC (3.2 g cm^{-3}). According to our first principles calculations, BP has a thermal expansion coefficient of 2.8 ×10^{-6} K^{-1} at 300 K close to that of Si (2.6 ×10^{-6} K^{-1}), indicating that BP can be readily integrated with Si-based devices. Cost efficient large-scale synthesis of BP powder can be realized by mechanochemical and self-propagating high temperature methods.[19]

BP has modest bandgap (2 eV) and the attendant relatively high dielectric constant[20] which facilitates the formation of shallow acceptors and donors. The highest mobility reported

in BP is 120 cm^2 s^{-1} V^{-1} and the lowest resistivity reported is 0.15 Ω cm at 300 K (see the last section in the Supporting Information).[21] BP can also be deposited as thin films on Si, SiC, and GaN substrates by chemical vapor deposition, metalorganic vapor phase epitaxy, and co-evaporation.[16, 22] Thus, BP is potentially useful not only as a heat spreader in high power microelectronics but also as an electronic device material for harsh environments.

Here, we report the temperature dependent thermal conductivity of BP crystals with natural B isotope concentration and isotopically enriched ^{11}BP crystals in the temperature range 120 K < T < 600 K using time-domain thermoreflectance (TDTR). Prior experimental work using TDTR was limited to BP with natural isotope concentration and temperatures below room temperature.[14] In this work, we developed a modified flux growth to synthesize high quality crystals of BP and ^{11}BP. The crystals are characterized by powder X-ray diffraction (P-XRD), single crystal X-ray diffraction (S-XRD), scanning transmission electron microscopy (STEM), and Raman spectroscopy. The room temperature thermal conductivities of BP (Λ_{nat}) and ^{11}BP (Λ_{pure}) are Λ_{nat} ≈490 W m^{-1} K^{-1} and Λ_{pure} ≈540 W m^{-1} K^{-1}, surpassing those of conventional high thermal conductivity materials such as Ag (≈430 W m^{-1} K^{-1}), Cu (≈400 W m^{-1} K^{-1}), BeO (≈370 W m^{-1} K^{-1}), and SiC (≈320 W m^{-1} K^{-1} for 4H SiC along c-axis), and only smaller than those of diamond, in-plane graphite, c-BN and BAs.[12, 23, 24, 9] The extra peak in the Raman spectrum of BP at 797 cm^{-1} observed in BP but not in ^{11}BP and previously assigned to LO-TO splitting is assigned to isotope disorder induced phonon scattering.

The measured Λ for BP and ^{11}BP show good agreement with our first principles calculations for T > 250 K. In our original theoretical work on BP, we used a cut-off for anharmonic force constants at the third nearest neighbor. In the present work, we found that extending the cut-off to tenth near-neighbors and incorporating zero-point motion and thermal expansion gives converged thermal conductivities that are reduced by approximately 15% from the previous calculations near room temperature.

We grew single crystals of BP with typical linear dimensions of 500-800 μm and well-formed facets, as shown in **Figure 1**b, following the synthesis procedure described in the Experimental Section. Powder XRD (P-XRD) data on crushed crystals, shown in Figure 1a, confirm a zinc blende structure with lattice parameter a = 4.5412(5) Å, consistent with previous results. [16, 25] The narrow FWHM of the P-XRD peaks indicates large crystalline domains and the absence of inhomogeneous strain fields in the samples. The P-XRD data are consistent with single crystal X-ray diffraction (S-XRD) data, see Figure 1c, where strong and round diffraction spots are visible. The S-XRD precession image shown in the Figure 1d is generated by integrating a large number of ω-scans. The precession images indicate that the sample microstructure is dominated by one domain. Weak reflections that are not consistent with a single crystal are also observed and are attributed to secondary domains. Quantitative analysis using the program TWINABS of data collected for one relatively small crystal with linear dimension of 300 μm reveals that the volume fraction of the primary domain is 97%; the fraction of the two secondary domains is approximately 3%.

To examine the atomic-scale structure, STEM images are acquired in a cross-section of a BP crystal prepared by focused ion beam (FIB). As shown in **Figure 2a**, an annular dark field STEM (ADF-STEM) image of the BP crystal is acquired along the [110] zone axis (see Figure 2b for schematic crystal structure along the same zone axis). The lattice shows no evident large-scale structural defects, such as grain boundaries or dislocations, consistent with the results from single crystal X-ray diffraction.

Room temperature Raman scattering spectra of BP and ^{11}BP crystals are presented in **Figure 3**. We include the calculated phonon density of states (pDOS) in **Figure 3** for comparison. The second order peaks of BP match well with singularities in the pDOS as shown in Figure 3c. The strong one-phonon line is generated by the longitudinal optical phonon at zone center, LO(Γ). The measured frequency of the LO(Γ) phonon is 826 cm^{-1} in BP and 819 cm^{-1} in ^{11}BP. The position of the one-phonon lines are in good agreement with previous

studies[26, 27] and our calculations (824 cm^{-1} in BP and 819 cm^{-1} in ^{11}BP). The shift of the LO(Γ) phonon peak between BP and ^{11}BP is mainly caused by the change in the average of the reduced atomic mass; the measured frequency shift is consistent with the change in the square root of the reduced mass (see the Supporting Information).

An extra peak appears at 797 cm^{-1} (overtone at ≈1598 cm^{-1}) next to the LO(Γ) phonon peak in BP natural isotope abundance and not in isotopically enriched ^{11}BP; this peak is labeled with an asterisk in **Figure 3**a. Previous studies have attributed the extra peak to Raman scattering from the transverse optical phonon at the Γ point, TO(Γ), as is often observed in zinc blende structure crystals.[14, 26, 28] However, our calculated value of the separation of the LO-TO phonon frequencies at the Γ point is only ≈7 cm^{-1}, much smaller than our observed frequency shift of 29 cm^{-1}. This discrepancy suggests that some other mechanism gives rise to the extra peak.

Isotope disorder breaks translational symmetry, partially relaxes the crystal momentum conservation rules, and allows extrema in the pDOS corresponding to Brillouin zone boundary phonons to appear in the one-phonon spectra. Such isotope-disorder induced Raman scattering typically appear as a shoulder on the LO(Γ) or TO(Γ) phonon peak in diamond-structured materials such as Si, Ge and diamond with modified isotopes.[29] Based on the calculated phonon dispersions (see Figure S2 in the Supporting Information), we attribute the 797 cm^{-1} peak in BP to isotopic disorder-induced scattering that involves LO phonons near either the X or K point, both of which have calculated frequencies close to 802 cm^{-1}. Further discussion of this assignment is included in the Supporting Information.

Representative TDTR data and model fitting for a sample at 300 K measured with a spot size w_0 = 10.4 μm and modulation frequency f = 9.3 MHz are shown in **Figure 4**a. We adjust two free parameters in the thermal model to fit the data: the Al/sample interface thermal conductance and the thermal conductivity of the ^{11}BP sample.[30] The diffusive thermal transport model based on Fourier's law assuming isotropic thermal conductivity are used for data fitting (see also Experimental and Theoretical Section).[30] The model curves with the best-

fit thermal conductivity of ^{11}BP changed by ±10% are also included to demonstrate the measurement sensitivity. The error bars labeled in Figure 4b, **Figure 5**a and 5b as well as **Figure S3** are uncertainty in Λ_A that propagates from the experimental noise and uncertainty in the fixed parameters in the Fourier's law model fitting. The typical interface thermal conductance as a function of temperature for Al/BP and Al/^{11}BP are plotted in Figure S3, which show room temperature values of approximately 180 MW m^{-2} K^{-1} and 220 MW m^{-2} K^{-1}, for Al/BP and Al/^{11}BP respectively.

In the analysis of TDTR measurements on high thermal conductivity crystals and semiconductor alloys, deviations from Fourier's law must be considered.[14, 31] Such deviation can result from ballistic phonon transport in the sample and from a mismatch in the distribution of phonons that carry heat across the metal/sample interface and the distribution of phonons that carry heat in the sample.[31, 32] In a recent study of Si, dilute SiGe alloys, and heavily boron doped Si,[31] the deviation from Fourier's law was shown to produce an apparent anisotropy in the thermal conductivity. A reduction in the characteristic length scales of the temperature gradients by increasing f or decreasing w_0 increases the percentage of low-frequency phonons with long mean-free-paths that are not in local equilibrium with the high-frequency phonons. Such effects cause the apparent thermal conductivity (Λ_A) derived from an isotropic diffusive thermal transport model using temperature gradients with small characteristic length scales to be smaller than thermal conductivity measured on large characteristic length scales. Further details are given in our prior publications.[31, 33] We use "systematic error" below to include the deviation from Fourier's law. This error originates from the deficiency of the model used to analyze the data and decreases the accuracy of our determination of the thermal conductivity.

To study deviations from Fourier's law in our TDTR measurements of BP and ^{11}BP crystals, we measured the apparent thermal conductivities (Λ_A) as a function of spot size w_0 at 128, 298, and 498 K, as shown in Figure 4b. Ballistic transport is most obvious at the lowest temperature of 128 K: Λ_A decreases by ≈30% in both BP and ^{11}BP as w_0 decreases from 26.5 to 2.7 μm. At

higher temperatures, the spot size dependence of Λ_A becomes weaker because the distribution of phonon-mean free-paths shifts to smaller lengths due to stronger phonon-phonon scattering (see Figure S4); the decrease of the thermal diffusivity also reduces the measurement sensitivity to in-plane heat transfer. In-plane heat transfer is more strongly affected by ballistic phonon effects than heat transfer normal to the surface.[31] The differences between Λ_A measured with w_0 = 26.5 and 10.4 μm are approximately 12% and 17% for BP and ^{11}BP at 128 K but less than 4% at 298 K and 498 K for both BP and ^{11}BP. The differences of 4% are smaller than the uncertainty of the thermal conductivity that propagates from uncertainties in the heat capacity per unit area of the Al transducer.

We used w_0 = 10.4 μm in the subsequent temperature dependent measurement (**Figure 5**b) because this smaller spot size provides better signal-to-noise than w_0 = 26.5 μm and systematic errors produced by deviations from Fourier's law should be small at T >300 K. As shown in Figure 4b, the spot size dependence of the apparent thermal conductivity in our data is consistent with recent experiments by Kang et al.[14]

We calculate the thermal conductivity accumulation function[34] for BP and ^{11}BP with no crystal imperfections at 128 K, 298 K, and 498 K (Figure S4) to gain additional insights into systematic errors created by the finite size of the laser spots. At 128 K, the accumulation extends to 10 μm, while at the two higher temperatures, most of the accumulation occurs below 1 μm, consistent with the observed spot size dependence of Λ_A.

Since the structure and concentration of defects in our BP samples is unknown, we did not attempt to incorporate the laser spot size effect in our first principles calculations. The effects of point defects on thermal conductivity are similar to the effects of the finite-size of the laser spot and we are not confident at this time that we can separate the two mechanisms by comparing experiment and theory. Consistent with prior work on a wide variety of single crystals, we do not observe modulation frequency dependence in the apparent thermal conductivity when we change the modulation frequency f between 1.1 and 9.3 MHz.[31, 33]

At 300 K, we measure Λ_{nat} = 490 ± 60 W m^{-1} K^{-1} for BP with a natural isotope abundance using a laser spot size of w_0 = 26.5 μm. This value is higher than what was obtained in laser-flash thermal diffusivity measurements by Kumashiro et. al. (400 W m^{-1} K^{-1})[13] and in steady-state measurements by Slack (360 W m^{-1} K^{-1} at 300 K).[12] Our measured values for BP differ by <10% from recent data for a BP single crystal measured with TDTR by Kang et. al. (460 W m^{-1} K^{-1}).[14] For isotopically modified ^{11}BP, Λ_{pure} = 540 ± 70 W m^{-1} K^{-1} at 300 K.

As shown in Figure 5a, the temperature dependent thermal conductivities of BP and ^{11}BP measured with w_0 = 10.4 μm show good agreement with our calculation above 250 K. In particular, calculated values at 300 K for BP and ^{11}BP are 486 W m^{-1} K^{-1} and 552 W m^{-1} K^{-1}, respectively, very close to the corresponding measured values. At high temperature, when phonon-phonon scattering dominates and the spot size dependence is weak, the isotope enrichment enhances Λ_{pure} by 10%, and 9% over Λ_{nat} at 300 K and 600 K, respectively. The measured isotope effect is in reasonably good agreement with the corresponding enhancements of 14% and 8% calculated from first principles. These new calculation results are approximately 15% lower than those reported in our prior work.[7] We discuss the differences in these results in more detail in the Experimental and Theoretical Section.

At low temperature, however, the experimental results deviate significantly from calculated values. We cannot however reliably separate reductions in the thermal conductivity generated by defect scattering from reductions in the apparent thermal conductivity created by the finite size of the laser spot.

As shown in Figure 5b, the thermal conductivities for BP and ^{11}BP between 300 and 600 K are much higher than common high thermal conductivity semiconductor materials including 4H SiC (cross plane direction,[35] which is consistent with Ref. [24]), bulk GaN[35] and Si.[36] Even at 600 K, the thermal conductivity of ^{11}BP maintains a high value of 200 ± 20 W m^{-1} K^{-1} , approximately three times that of Si at the same temperature.

We plot in Figure 5c, the measured Λ multiplied by temperature, i.e. ΛT, as a function of measurement temperature to compress the range of the data and more clearly present the differences between theory and experiment. In this figure, a $\Lambda \propto T^{-1}$ dependence would appear as a horizontal line. The slopes of our experimental data are steeper than the typical T^{-1} behavior of insulating crystals with Λ_{pure} and Λ_{nat} both showing a dependence, $\Lambda \propto T^{-1.4}$, in the range 300 K < T < 600 K. The measured results show good agreement with the first principles calculations, particularly at intermediate temperatures 250 K < T < 400 K. In fact, the T^{-1} dependence of Λ for three-phonon limited scattering is expected for temperatures above the Debye temperature.[37] The more rapid rise than T^{-1} seen in both measured and calculated data below 600 K is in part a consequence of being below the Debye temperature of BP (≈1100 K)[7] where the decrease in resistive umklapp scattering gives a steeper temperature dependence. In addition, the increased lattice constant with increasing T softens optic phonon frequencies, which in turn increases three-phonon scattering rates between heat-carrying acoustic phonons and optic phonons. This further lowers the thermal conductivity beyond that obtained from ignoring thermal expansion.

The slightly higher calculated values of Λ_{pure} and Λ_{nat} suggest the presence of a small concentration of defects. To investigate this, we included additional point defect scattering in our theoretical calculations where substitutional impurities on the B and P sites were treated as mass defects in the crystal within the Born approximation. We placed the point defects with equal mass disorder parameters[38] on B and P sites and fit the experimental data from 300 K to 600 K as shown in Figure 5c. For BP, the natural isotope mix of the boron atom gives a mass disorder parameter on B of $g_{iso} = 1.36 \times 10^{-3}$. Using added point defect scattering strengths with mass disorder parameter $g_{PD} = 5.19 \times 10^{-5}$, and 4.05×10^{-5} in BP and ^{11}BP respectively, we obtain an improved match between the theoretical calculations and experimental data around

and above 200 K. We note that the values for g_{PD} in both cases are quite small reflecting the high quality of the samples.

In summary, we report a time-domain thermoreflectance study of the thermal conductivity in high quality crystals of BP with natural isotopic abundanc and isotopically enriched ^{11}BP crystals grown with flux method between 120 and 600 K. The thermal conductivities of BP and ^{11}BP are measured to be ≈490 and ≈540 W m^{-1} K^{-1}, respectively at 300 K, exceeding those of conventional high thermal conductivity materials. The measured data shows excellent agreement with first principles theoretical calculations over a wide temperature range, reflecting the high quality of the measured samples. Based on S-XRD and STEM analysis, as well as a comparison between the theoretical and experimental data, we attribute the slightly lower Λ in the BP and ^{11}BP compared with theoretical prediction near 300 K to weak phonon point defect scattering. This work provides benchmark knowledge about the thermal transport properties and the isotope scattering effect in BP and ^{11}BP, thus advancing their potential for a broad range of applications, and contributing to understanding and future development of high thermal conductivity materials through isotope enrichment.

Experimental and Theoretical Section

Single crystal growth: Crystals of BP and ^{11}BP were synthesized through the modified flux method using copper phosphide as the flux. Starting materials of natural boron powder (99.99%, Alfa Aesar) or enriched ^{11}B powder (99%, Cambridge Isotope), red phosphorus lump (99.999%, Alfa Aesar), and copper powder (99.99%, Alfa Aesar), with the mass ratio 1:10:50, were double sealed in fused quartz tubes under vacuum. The assembly was placed in the horizontal tube furnace with starting materials at the hot end, slowly heated up at a rate of 5 °C/h to 1250 °C for 3 days, then slowly cooled down to 990 °C at a rate of 3 °C/h. After reaching 990 °C, the furnace heaters were turned off and the furnace was allowed to rapidly cool to room temperature.

After reaction, dark red crystals, with typical linear dimensions of 500 μm, were obtained after aqua regia cleaning, followed by acetone and isopropanol wash. Different ratios of starting materials and temperature profiles have been tested for the optimization of the crystal growth. It is worthwhile to mention that a tube furnace with temperature gradient (> 300 °C) from hot end to cold end was found to be more helpful than the box furnaces with uniform temperature gradient during the crystal growth for the quality and size of the grown crystals.

X-ray Diffraction: Single crystal diffraction measurements were performed using a Bruker Apex DUO single crystal diffractometer equipped with a 4K CCD APEX II detector using Cu Kα radiation. Structure determination and refinements were carried out using the Bruker Apex II software package. Domain analysis on the single diffraction data were performed using the program TWINABS. Powder diffraction measurements were performed on the Rigaku Smartlab.

STEM: Annular dark field STEM images were acquired with an aberration corrected Titan Themis Z STEM operated at 80 kV. 20 frames of the same region, each acquired with 3.05 sec, were cross-correlated to reduce scan noise and sample drift and then summed to produce the final image in Figure 2a. The gamma (intensity scaling) in the windowed Fourier transform in Figure 2c has been adjusted to make the spots more visible. The specimens for STEM study were prepared using FEI Helios 600i DualBeam focused ion beam (FIB), with a standard lift-out procedure and a final milling step of 2 kV to reduce surface damage.

Raman: The Raman spectroscopy measurements were performed using an Acton Insight spectrometer (Princeton Instruments). The excitation wavelength is 488 nm from a Spectra-Physics Cyan (CDRH) solid state laser. A power of ≈10 mW is used to avoid excessive sample heating. The backscattered signal was collected through a 20× objective (N.A. = 0.4) with laser spot radius ≈5 μm at the sample surface and dispersed by a 1200 gmm^{-1} grating. The instrument resolution we obtained by deconvoluting the well understood Si one-phonon 520 cm^{-1} peak is around 3.2 cm^{-1}.[39]

Time-domain thermoreflectance (TDTR): Time-domain thermoreflectance (TDTR) was used to measure the thermal conductivity of BP and ^{11}BP.[30, 40] Prior to the measurement, the sample was cleaned by ultrasonication in ethanol to remove particles and hydrocarbon contamination that adsorb on sample surface during shipping. The sample was then mounted onto a 0.025 mm copper foil with PELCO® silver paint and coated with an Al transducer layer with a thickness of approximately 80 nm by magnetron sputtering. The copper foil with sample was then mounted onto the onto a commercial Instec® vacuum heater stage using PELCO® silver paint for temperature dependent TDTR measurement. The stage chamber is pumped with a turbo-molecular pump to maintain a pressure lower than $< 7.5 \times 10^{-4}$ Torr in the temperature dependent measurement for cooling and prevent sample oxidation at high temperature. Crystal facets with smooth surface with a reflectivity > 95% of that of the silicon wafer were selected for the TDTR characterization.

In a TDTR measurement, a train of 785 nm optical pulses at a repetition rate of 74.86 MHz, generated by a mode-locked Ti:Sapphire laser, were split into separate pump and probe beams with the optical path of the pump beam controlled by a mechanical delay stage. The pump beam was modulated at a frequency of f = 9.3 MHz by an electro-optical modulator. The pump and probe beams were typically focused on the sample through a 5× objective lens to a $1/e^2$ intensity radius of ≈10.4 μm in the temperature dependent measurement. Objective lenses with different magnification were used for the laser spot size TDTR measurement. The total beam power of 30 mW created a steady-state temperature rise of <1 K at all temperature range. The changes in the intensity of the reflected probe beam due the thermoreflectance of the Al transducer created by the pump beam were measured using lock-in detection. The ratio of the in-phase (V_{in}) and out-of-phase (V_{out}) signal from the lock-in amplifier is then fit to a thermal diffusion model obtained from an analytical solution for heat flow in a layered structure based on Fourier's law.[30]

The diffusive thermal transport model used for TDTR data fitting included parameters for the thermal conductivity, heat capacity, and thickness of the Al transducer layers and the BP and ^{11}BP sample as well as the as the Al/sample interface thermal conductance. We assumed the thermal conductivity of the sample is isotropic in the analysis. The thickness of Al thin film was obtained from picosecond acoustics using a longitudinal speed of sound 6.42 nm ps^{-1}.[41] The thermal conductivity of the Al thin film was calculated using the Wiedemann-Franz law and the electrical resistance of the Al film deposited on a 500 nm SiO_2 on Si reference sample placed next to the sample in sputtering. The analysis was not sensitive to the thin Al transducer layer thermal conductivity.[42] The heat capacity of Al is taken from literature values.[43]

We measured the volumetric heat capacity *C* of the sample by a Quantum Design Physical Property Measurement System (PPMS) from 10 to 393 K (see Figure S1). The volumetric heat capacity at constant pressure, C_P, was also calculated using $C_P = C_V + \alpha^2 BT$. The constant volume heat capacity C_V was obtained by integrating the phonon density of states derived from first principles calculation). A literature value was used for the bulk modulus *B*,[44] while the volumetric thermal expansion coefficient α was obtained from a first principles calculation. The calculated C_P is in good agreement with the measured result with deviation of less than 3% between 100 and 393 K and is consistent with previous literature experimental data at higher temperature. We used the calculated C_P in the TDTR data analysis for measurement between 120 K and 600 K.

The thermal conductivity data for 4H-SiC is measured on semi-insulating wafer sample from TankeBlue® and the GaN data are measured on undoped n-type sample provided by Kyma®.

First principles calculations: First principles lattice thermal conductivity was calculated by solving the Peierls-Boltzmann equation (PBE) as described, for example, in references.[45] Harmonic and anharmonic force constants (IFCs) were calculated using density functional

theory. We used a plane wave and pseudopotential based approach as implemented in Quantum Espresso (QE).[46] Norm conserving pseudopotentials generated with the Bachelet-Hamann-Schlüter method[47] and the local density approximation (LDA) of the exchange correlation functional as parameterized by Perdew and Zunger were used.[48] We set an energy cutoff of 100 Ry to ensure the accurate calculation of forces. The crystal structure was fully relaxed at each temperature within the quasi-harmonic approximation (QHA).[49] As detailed in the Supplementary Information, the QHA, incorporates both zero-point and thermal motion of the atoms in determining the lattice constant at each temperature that minimizes the Helmholtz free energy. The obtained lattice constant at 300 K of 4.486 Å is approximately 1.2% smaller than the experimental one and is typical of over-binding in the LDA. The harmonic IFCs were calculated at each temperature on an 8×8×8 **q** grid within density functional perturbation theory as implemented in QE. From these, phonon frequencies and eigenvectors were determined. The Born effective charge and dielectric constant at 300 K were: Z^B = 0.67 and ϵ_∞ = 9.27, respectively. The reduced effective charge, $Z^B/\sqrt{\epsilon_\infty}$ is in good agreement with obtained values in previous calculations.[50] Third-order anharmonic IFCs were computed with the supercell/finite difference scheme,[51] using a 5×5×5 supercell with up to 10th nearest neighbor interactions. We modeled isotopes and other assumed point defects as producing mass disorder that scatters phonons, following the formulation of Tamura.[38] The disorder is characterized by parameter, $g(b)$, where b labels either the B or the P site. The PBE was solved iteratively using up to a 48×48×48 **q** grid.

We note that calculated room temperature thermal conductivity values for BP presented in this work are about 15% smaller than values published previously in Ref. [7] There, the values obtained were too high because (i) third-order IFCs were used whose range (third-nearest neighbor) was insufficient to capture the full three-phonon scattering strengths. We have used third-order IFCs that extend to tenth nearest neighbor in the present work; (ii) the larger lattice

constant in the QHA calculations is increased by both zero-point vibrations and thermal motion (see the Supporting Information). This gives softer optic phonons that increase phonon-phonon scattering and reduce the thermal conductivity, as described above.

Supporting Information
Supporting Information is available from the Wiley Online Library or from the author.

Acknowledgements
Qiye Zheng and Sheng Li contributed equally to this work. This work is supported by the Office of Naval Research MURI Award N00014-16-1-2436. Thermal conductivity, Raman, and STEM was carried out in part in Frederick Seitz Materials Research Laboratory (MRL) at the University of Illinois at Urbana-Champaign. Chunhua Li and David Broido also acknowledge support from the Boston College Linux Cluster. Sheng Li, Xiaoyuan Liu and Bing Lv also acknowledge support from US Air Force Office of Scientific Research Grant No. FA9550-15-1-0236 and the start-up funds from University of Texas at Dallas.

References

[1] M. M. Waldrop, Nature 2016, 530, 144; P. Ball, Nature News 2012, 492, 174; A. L. Moore, L. Shi, Materials Today 2014, 17, 163; A. Bar-Cohen, P. Wang, Journal of Heat Transfer 2012, 134, 051017.
[2] S. V. Garimella, A. S. Fleischer, J. Y. Murthy, A. Keshavarzi, R. Prasher, C. Patel, S. H. Bhavnani, R. Venkatasubramanian, R. Mahajan, Y. Joshi, B. Sammakia, B. A. Myers, L. Chorosinski, M. Baelmans, P. Sathyamurthy, P. E. Raad, IEEE Transactions on Components and Packaging Technologies 2008, 31, 801.
[3] S. V. Garimella, L. T. Yeh, T. Persoons, IEEE Transactions on Components, Packaging and Manufacturing Technology 2012, 2, 1307; A. Shehabi, S. Smith, D. Sartor, R. Brown, M. Herrlin, J. Koomey, E. Masanet, N. Horner, I. Azevedo, W. Lintner, 2016.
[4] K. N. Tu, Microelectronics Reliability 2011, 51, 517; W. Huang, K. Rajamani, M. R. Stan, K. Skadron, IEEE Micro 2011, 31, 16.
[5] S. Kakaç, H. Yüncü, K. Hijikata, *Cooling of electronic systems*, Vol. 258, Springer Science & Business Media, 2012. I. Chowdhury, R. Prasher, K. Lofgreen, G. Chrysler, S. Narasimhan, R. Mahajan, D. Koester, R. Alley, R. Venkatasubramanian, Nature Nanotechnology 2009, 4, 235; V. Sahu, Y. K. Joshi, A. G. Fedorov, Nanoscale and Microscale Thermophysical Engineering 2009, 13, 135; J.-T. Cheng, C.-L. Chen, Experiments in fluids 2010, 49, 1349.
[6] S. V. Kidalov, F. M. Shakhov, Materials 2009, 2, 2467; C.-Y. Guo, X.-B. He, S.-B. Ren, X.-H. Qu, Rare Metals 2016, 35, 249.
[7] L. Lindsay, D. A. Broido, T. L. Reinecke, Physical Review Letters 2013, 111, 025901.
[8] T. Feng, L. Lindsay, X. Ruan, Physical Review B 2017, 96, 161201.
[9] B. Lv, Y. Lan, X. Wang, Q. Zhang, Y. Hu, A. J. Jacobson, D. Broido, G. Chen, Z. Ren, C.-W. Chu, Applied Physics Letters 2015, 106, 074105; F. Tian, B. Song, B. Lv, J. Sun, S. Huyan, Q. Wu, J. Mao, Y. Ni, Z. Ding, S. Huberman, T.-H. Liu, G. Chen, S. Chen, C.-W. Chu, Z. Ren, Applied Physics Letters 2018, 112, 031903; J. Kim, D. A. Evans, D. P. Sellan, O. M. Williams, E. Ou, A. H. Cowley, L. Shi, Applied Physics Letters 2016, 108, 201905; S.

Li, Q. Zheng, Y. Lv, X. Liu, X. Wang, P. Y. Huang, D. G. Cahill, B. Lv, Science 2018, eaat8982; F. Tian, B. Song, X. Chen, N. K. Ravichandran, Y. Lv, K. Chen, S. Sullivan, J. Kim, Y. Zhou, T.-H. Liu, M. Goni, Z. Ding, J. Sun, G. A. G. U. Gamage, H. Sun, H. Ziyaee, S. Huyan, L. Deng, J. Zhou, A. J. Schmidt, S. Chen, C.-W. Chu, P. Y. Huang, D. Broido, L. Shi, G. Chen, Z. Ren, Science 2018, aat7932; J. S. Kang, M. Li, H. Wu, H. Nguyen, Y. Hu, Science 2018, eaat5522.

[10] N. H. Protik, J. Carrete, N. A. Katcho, N. Mingo, D. Broido, Physical Review B 2016, 94, 045207; S. Li, Q. Zheng, Y. Lv, X. Liu, X. Wang, P. Y. Huang, D. G. Cahill, B. Lv, Science 2018, eaat8982.

[11] T. D. O. N. V. Novikov, A. A. Shul'zhenko, A. P. Podoba, A. N. Sokolov, and I. A. Petrusha, Dopov. Akad. Nauk Ukr. RSR, Ser. A: Fiz.-Tekh. Mat. Nauki 1983, 72.

[12] G. A. Slack, Journal of Physics and Chemistry of Solids 1973, 34, 321.

[13] Y. Kumashiro, T. Mitsuhashi, S. Okaya, F. Muta, T. Koshiro, Y. Takahashi, M. Mirabayashi, Journal of Applied Physics 1989, 65, 2147.

[14] J. S. Kang, H. Wu, Y. Hu, Nano Letters 2017, 17, 7507.

[15] D. Broido, L. Lindsay, T. Reinecke, Physical Review B 2013, 88, 214303; G. A. Slack, Physical Review 1957, 105, 829; T. Geballe, G. Hull, Physical Review 1958, 110, 773; C. Glassbrenner, G. A. Slack, Physical Review 1964, 134, A1058; J. R. Olson, R. O. Pohl, J. W. Vandersande, A. Zoltan, T. R. Anthony, W. F. Banholzer, Physical Review B 1993, 47, 14850.

[16] Y. Kumashiro, Journal of Materials Research 1990, 5, 2933.

[17] Y. Kumashiro, Y. Okada, S. Gonda, Journal of Crystal Growth 1984, 70, 507; T. Takao, T. Mitsuharu, S. Katsufusa, Japanese Journal of Applied Physics 1976, 15, 2235; V. L. Solozhenko, O. O. Kurakevych, Y. Le Godec, A. V. Kurnosov, A. R. Oganov, Journal of Applied Physics 2014, 116, 033501; A. Rendtel, B. Moessner, K. A. Schwetz, *Hardness and hardness determination in silicon carbide materials*, John Wiley & Sons, Inc, 2008; S. Dub, P. Lytvyn, V. Strelchuk, A. Nikolenko, Y. Stubrov, I. Petrusha, T. Taniguchi, S. Ivakhnenko, Crystals 2017, 7, 369.

[18] U. R. K. Lagudu, in *Advances in Chemical Mechanical Planarization (CMP)*, (Ed: S. Babu), Woodhead Publishing, 2016, 169.

[19] V. A. Mukhanov, D. Vrel, P. S. Sokolov, Y. Le Godec, V. L. Solozhenko, Dalton Transactions 2016, 45, 10122; V. A. Mukhanov, P. S. Sokolov, Y. L. Godec, V. L. Solozhenko, Journal of Superhard Materials 2013, 35, 415.

[20] R. J. Archer, R. Y. Koyama, E. E. Loebner, R. C. Lucas, Physical Review Letters 1964, 12, 538; V. A. Fomichev, I. I. Zhukova, I. K. Polushina, Journal of Physics and Chemistry of Solids 1968, 29, 1025; *Group IV Elements, IV-IV and III-V Compounds. Part b - Electronic, Transport, Optical and Other Properties*, (Eds: O. Madelung, U. Rössler, M. Schulz), Springer Berlin Heidelberg, Berlin, Heidelberg 2002, 1.

[21] B. Stone, D. Hill, Physical Review Letters 1960, 4, 282; Y. Kumashiro, Journal of Materials Research 2011, 5, 2933.

[22] T. Chu, J. Jackson, A. Hyslop, S. Chu, Journal of Applied Physics 1971, 42, 420; B. Padavala, C. Frye, Z. Ding, R. Chen, M. Dudley, B. Raghothamachar, N. Khan, J. Edgar, Solid State Sciences 2015, 47, 55; K. Shohno, M. Takigawa, T. Nakada, Journal of Crystal Growth 1974, 24, 193; M. Odawara, T. Udagawa, G. Shimaoka, Applied surface science 2005, 244, 289; Y. Kumashiro, K. Nakamura, T. Enomoto, M. Tanaka, Journal of Materials Science: Materials in Electronics 2011, 22, 966.

[23] W. M. Haynes, *CRC Handbook of Chemistry and Physics, 96th Edition*, CRC Press, 2015; O. Nilsson, H. Mehling, R. Horn, J. Fricke, R. Hofmann, S. G. Müller, R. Eckstein, D. Hofmann, High Temperatures. High Pressures 1997, 29, 73; G. A. Slack, R. A. Tanzilli, R. Pohl, J. Vandersande, Journal of Physics and Chemistry of Solids 1987, 48, 641; L. Wei, P. K. Kuo, R. L. Thomas, T. R. Anthony, W. F. Banholzer, Physical Review Letters 1993, 70,

3764; G. A. Slack, Physical Review 1962, 127, 694; L. Vel, G. Demazeau, J. Etourneau, Materials Science and Engineering: B 1991, 10, 149; G. A. Slack, S. B. Austerman, Journal of Applied Physics 1971, 42, 4713.
[24] X. Qian, P. Jiang, R. Yang, Materials Today Physics 2017, 3, 70.
[25] W. Katherine, L. Kathleen, K. Kirill, Materials Research Express 2016, 3, 074003.
[26] J. A. Sanjurjo, E. López-Cruz, P. Vogl, M. Cardona, Physical Review B 1983, 28, 4579; B. Padavala, C. D. Frye, X. Wang, Z. Ding, R. Chen, M. Dudley, B. Raghothamachar, P. Lu, B. N. Flanders, J. H. Edgar, Crystal Growth & Design 2016, 16, 981.
[27] Y. Kumashiro, Y. Okada, H. Okumura, Journal of Crystal Growth 1993, 132, 611.
[28] Y. Cheng, C. Jin, F. Gao, X. Wu, W. Zhong, S. Li, P. K. Chu, Journal of Applied Physics 2009, 106, 123505; S. Reich, A. Ferrari, R. Arenal, A. Loiseau, I. Bello, J. Robertson, Physical Review B 2005, 71, 205201.
[29] H. Fuchs, P. Etchegoin, M. Cardona, K. Itoh, E. Haller, Physical review letters 1993, 70, 1715; F. Widulle, T. Ruf, M. Konuma, I. Silier, M. Cardona, W. Kriegseis, V. I. Ozhogin, Solid State Communications 2001, 118, 1; J. Spitzer, P. Etchegoin, M. Cardona, T. R. Anthony, W. F. Banholzer, Solid State Communications 1993, 88, 509.
[30] D. G. Cahill, Review of Scientific Instruments 2004, 75, 5119.
[31] R. B. Wilson, D. G. Cahill, Nature Communications 2014, 5, 5075.
[32] D. Ding, X. Chen, A. J. Minnich, Applied Physics Letters 2014, 104, 143104; K. T. Regner, J. P. Freedman, J. A. Malen, Nanoscale and Microscale Thermophysical Engineering 2015, 19, 183; R. Cheaito, J. T. Gaskins, M. E. Caplan, B. F. Donovan, B. M. Foley, A. Giri, J. C. Duda, C. J. Szwejkowski, C. Constantin, H. J. Brown-Shaklee, J. F. Ihlefeld, P. E. Hopkins, Physical Review B 2015, 91, 035432; A. J. Minnich, J. Johnson, A. Schmidt, K. Esfarjani, M. Dresselhaus, K. A. Nelson, G. Chen, Physical review letters 2011, 107, 095901.
[33] R. B. Wilson, D. G. Cahill, Applied Physics Letters 2015, 107, 203112.
[34] F. Yang, C. Dames, Physical Review B 2013, 87, 035437.
[35] Q. Zheng, D. G. Cahill, unpublished 2018.
[36] W. Fulkerson, J. P. Moore, R. K. Williams, R. S. Graves, D. L. McElroy, Physical Review 1968, 167, 765.
[37] G. Leibfried, E. Schlömann, *Wärmeleitung in Elektrisch Isolierenden Kristallen, von Günther Leibfried und Ernst Schlömann*, Vandenhoeck und Ruprecht, 1954.
[38] S. Tamura, Physical Review B 1984, 30, 849.
[39] J. P. Feser, J. S. Sadhu, B. P. Azeredo, K. H. Hsu, J. Ma, J. Kim, M. Seong, N. X. Fang, X. Li, P. M. Ferreira, S. Sinha, D. G. Cahill, Journal of Applied Physics 2012, 112, 114306.
[40] K. Kang, Y. K. Koh, C. Chiritescu, X. Zheng, D. G. Cahill, Review of Scientific Instruments 2008, 79, 114901.
[41] D. G. Cahill, F. Watanabe, Physical Review B 2004, 70, 235322.
[42] J. Yang, E. Ziade, A. J. Schmidt, Review of Scientific Instruments 2016, 87, 014901.
[43] E. H. Buyco, F. E. Davis, Journal of Chemical & Engineering Data 1970, 15, 518.
[44] V. L. Solozhenko, O. O. Kurakevych, Y. Le Godec, A. V. Kurnosov, A. R. Oganov, Journal of Applied Physics 2014, 116, 033501; *Group IV Elements, IV-IV and III-V Compounds. Part b - Electronic, Transport, Optical and Other Properties*, (Eds: O. Madelung, U. Rössler, M. Schulz), Springer Berlin Heidelberg, Berlin, Heidelberg 2002, 1.
[45] D. Broido, M. Malorny, G. Birner, N. Mingo, D. Stewart, Applied Physics Letters 2007, 91, 231922; A. Ward, D. Broido, D. A. Stewart, G. Deinzer, Physical Review B 2009, 80, 125203.
[46] P. Giannozzi, S. Baroni, N. Bonini, M. Calandra, R. Car, C. Cavazzoni, D. Ceresoli, G. L. Chiarotti, M. Cococcioni, I. Dabo, Journal of physics: Condensed matter 2009, 21, 395502.
[47] G. Bachelet, D. Hamann, M. Schlüter, Physical Review B 1982, 26, 4199.

[48] J. P. Perdew, A. Zunger, Physical Review B 1981, 23, 5048.
[49] A. A. Maradudin, E. W. Montroll, and G. H. Weiss, Theory of Lattice Dynamics in the Harmonic Approximation (Academic, New York, 1963), Vol. 3 of Solid-state physics.
[50] Thomas Pletl, Pasquale Pavone, Ulrike Engel, Dieter Strauch, Physica B 263-264, 1999, 392.
[51] W. Li, L. Lindsay, D. Broido, D. A. Stewart, N. Mingo, Physical Review B 2012, 86, 174307.

Figures and figure captions

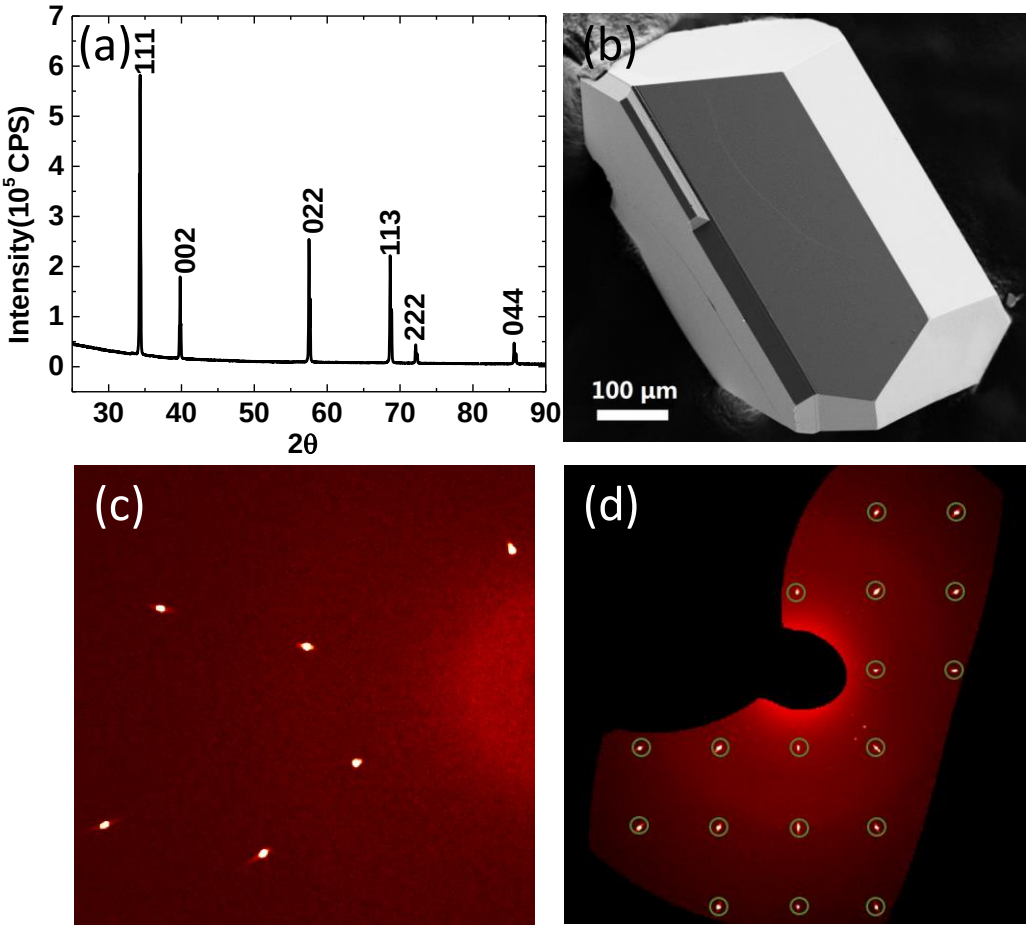

Figure 1. a) Powder X-ray diffraction pattern with Miller indices on crushed BP crystals. b) A representative SEM image of selected BP crystals. c) one diffraction frame from single crystal X-ray diffraction showing good crystallinity of the selected BP crystal. d) Precession images of *(h0l)* zone by using a set of measured ω-scan frames (1270) where the circled strong spots are from one domain while the weak unindexed spots (<3%) are from other domains.

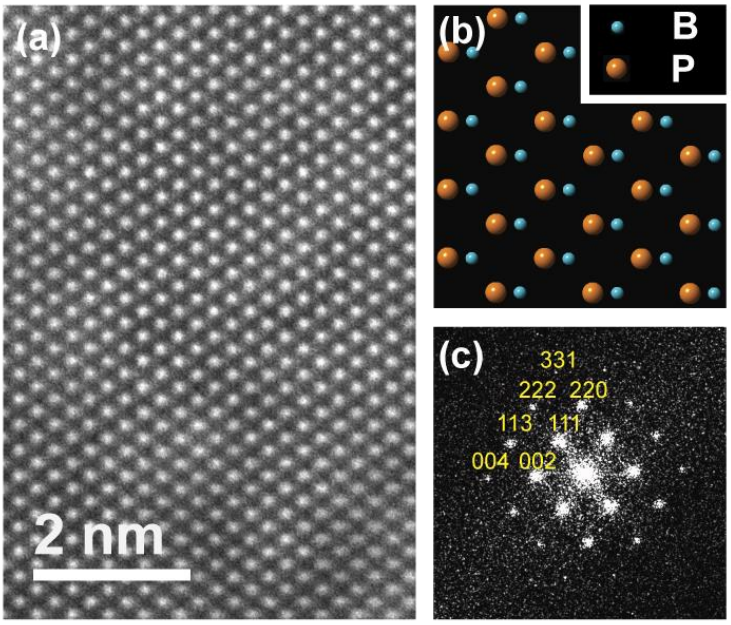

Figure 2. a) Annular dark field STEM image of a BP crystal along the [110] zone axis, showing the zinc blende crystal structure. The contrast of the STEM image is proportional to Z^{γ} (where $1.5 < \gamma < 2$), and thus the bright spots primarily contain contrast from phosphorus atom columns. b) Cartoon of BP crystal structure along the [110] zone axis. c) Windowed Fourier transform of the STEM image in a).

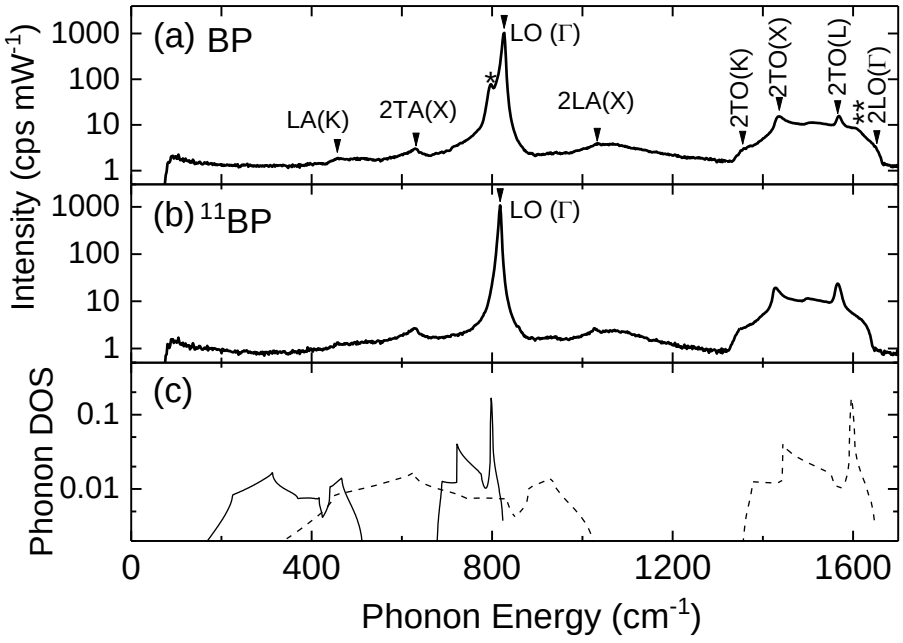

Figure 3. Room temperature Raman scattering spectra of a) BP and b) ^{11}BP with y-axis unit of counts per second per milliwatt. c) The phonon density of states (pDOS) of isotopically mixed BP (solid line) and the same (pDOS) scaled by a factor of two (dash line). The attribution of most Raman peaks to corresponding one phonon or combination modes are labeled with

solid triangles in a). The asterisk labels the peak at 797 cm^{-1} that we attribute to isotopic disorder induced scattering with the LO phonon at the X (or K) point of Brillouin zone. This feature was previously identified in literature as arising from the TO(Γ) phonon. The Raman spectrum shoulder labeled with two asterisks is the overtone of the LO(X or K) phonon.

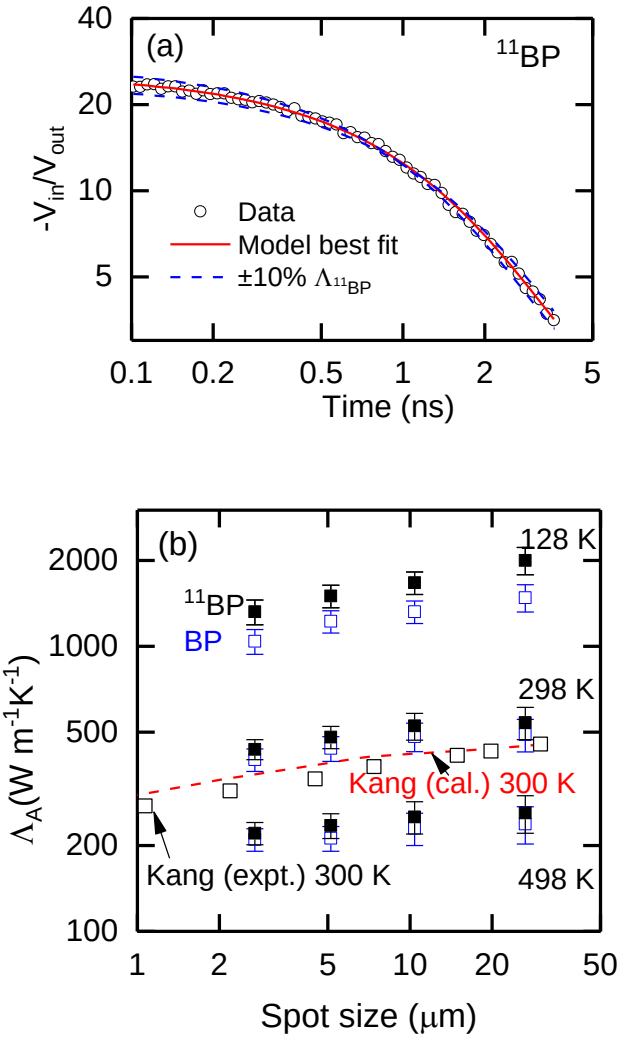

Figure 4. a) Example TDTR data: $-V_{in}/V_{out}$ *vs*. delay time for ^{11}BP with 89 nm Al transducer layer at RT measured with spot size w_0 = 10.4 μm and modulation frequency f = 9.3 MHz (black open circles) compared to the predictions of the thermal transport model described in the text (red solid lines). V_{in} and V_{out} are the in-phase and out-of-phase signal, respectively from the lock-in amplifier. Model curves calculated using the best-fit thermal conductivity changed by

±10% (dashed lines) are also plotted. b) Spot-size dependent apparent thermal conductivity from TDTR for BP (blue open circles) and ^{11}BP (black filled squares) at three different temperatures of 128, 298, and 498 K, with f = 9.3 MHz. The experimental (black open squares) and calculated (red dashed line) results for natural BP from previous literature at 300 K are also included for comparison.[14]

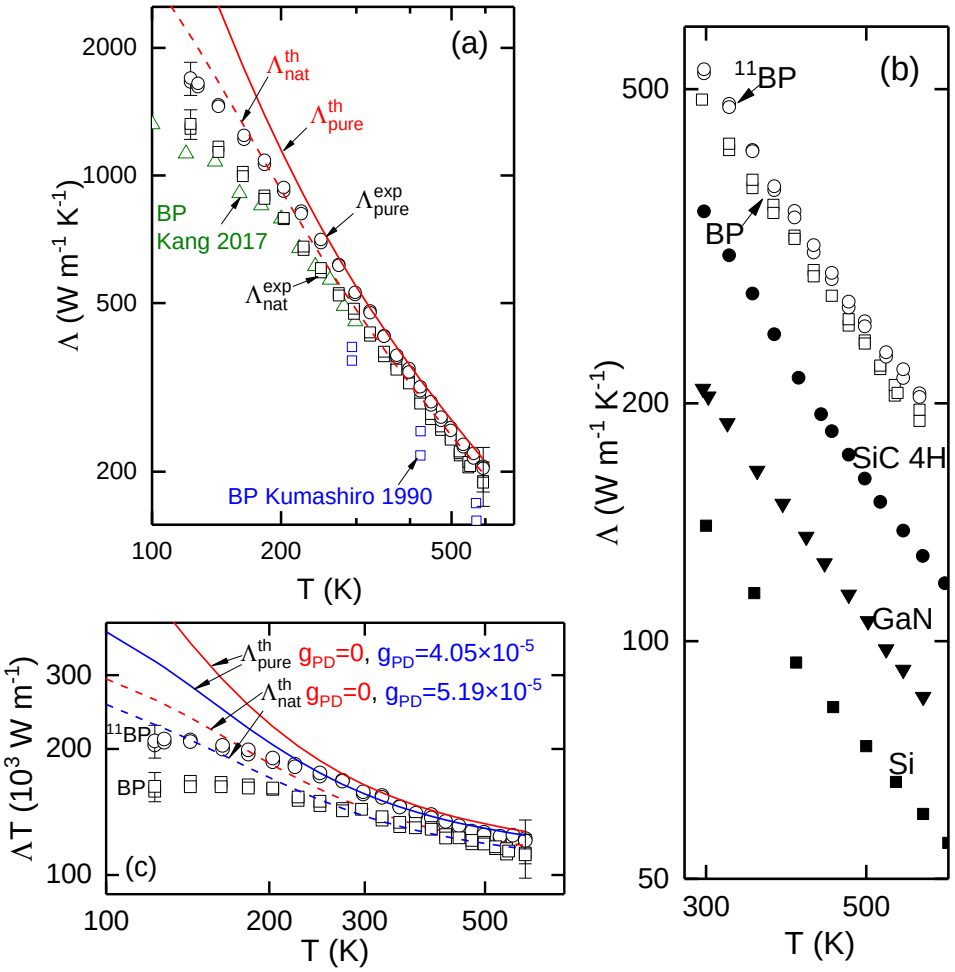

Figure 5. a) Temperature dependent thermal conductivity of BP (black open squares) and isotopically pure ^{11}BP (black open circles) from 120 to 600 K measured using w_0 = 10.4 μm and f = 9.3 MHz. The first principles BTE calculation results for BP (red dashed line; includes three-phonon and phonon-isotope scattering), and ^{11}BP (red line; includes only three-phonon scattering) are presented for comparison. Representative error bars are shown at 120 K and 600 K. We also include the literature data of BP thin film by Kumashiro et al. (blue open squares),[13]

and BP crystal by Kang et al. (green open triangles).[14] b) Thermal conductivity between 300 to 600 K for BP and ^{11}BP compared with 4H SiC (cross plane direction),[35] bulk GaN,[35] and Si.[36] c) Thermal conductivity data of our samples in a) multiplied by temperature vs. temperature (symbols and red lines have the same indications as a)). We also include first principles BTE calculation results similar to a) but with extra point defects with equal mass disorder parameters g_{PD} on B and P sites for BP (blue dashed line; $g_{PD} = 5.19 \times 10^{-5}$) and ^{11}BP (blue line; $g_{PD} = 4.05 \times 10^{-5}$).

The table of contents entry:
Thermal conductivities (Λ) of high quality natural abundance BP and isotopically-enriched ^{11}BP single crystals measured from 120 to 600 K using time-domain thermoreflectance shows good agreement with theoretical calculation. Their intrinsic high Λ, 490 (BP) and 540 W m^{-1} K^{-1} (^{11}BP) at 300 K, surpass many conventional high Λ materials which suggests their potential applications in heat dissipation and high-power electronics.

Keyword: high thermal conductivity material, isotope enrichment effect, time-domain thermoreflectance, first principles calculation, Raman spectroscopy

Qiye Zheng, Sheng Li, Chunhua Li, Yinchuan Lv, Xiaoyuan Liu, Pinshane Huang, David A. Broido, Bing Lv, and David G. Cahill**

Title: High thermal conductivity in isotopically enriched cubic boron phosphide

ToC figure

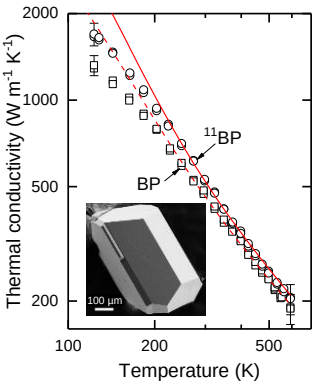

Supporting Information

High thermal conductivity in isotopically enriched cubic boron phosphide

Qiye Zheng, Sheng Li, Chunhua Li, Yinchuan Lv, Xiaoyuan Liu, Pinshane Huang, David A. Broido, Bing Lv, and David G. Cahill**

Heat capacity of BP

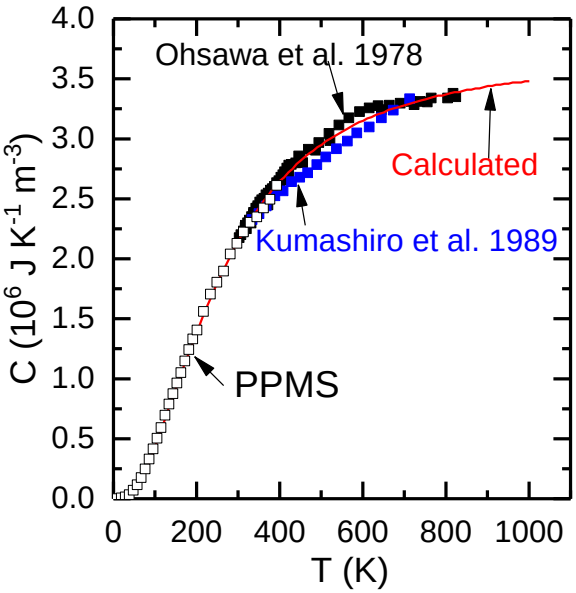

Figure S1. Heat capacity of BP C_p measured by PPMS (black open square) and calculated from phonon DOS and quasi-harmonic term as described in method part of the main text (red line) in comparison with literature data (blue and black filled square).[1]

Figure S1 shows the heat capacity per unit volume for BP from our calculations and literature experiments.[1] At 300 K, the heat capcity of BP is 2.13×10^6 J m^{-3} K^{-1} (0.74 J g^{-1} K^{-1}) which is close to that of Si (0.71 J g^{-1} K^{-1}) comparable with Al (0.9 J g^{-1} K^{-1}) and larger than that of Cu (0.38 J g^{-1} K^{-1}) at room temperature. We do not plot the heat capacity in the unit of J g^{-1} K^{-1} for two reasons. In transient heat flow, the relevant thermal properties are the thermal diffusivity, $D = \Lambda/\rho C_p'$, and thermal effusivity, $E = (\Lambda\rho C_p')^{1/2}$, where ρ is the mass density in the unit of g m^{-3}, if heat capcity C' is in the unit of J g^{-1} K^{-1}. Thus, only heat capacity per unit volume, $C_p = C_p'\rho$ in the unit of J m^{-3} K^{-1}, is relevant. For steady state heat transfer which is the case for heat spreader application, heat capacity does not matter at all.

First principles calculations in the quasi-harmonic approximation

In the quasi-harmonic approximation (QHA), the Helmholz free energy, *F*, is approximated as: $F_{QHA}(a,T) \approx F_0(a) + F_{vib}(a,T)$ where F_0 is the static internal energy of the lattice atoms in their equilibrium positions, and F_{vib} is the vibrational free energy given by: $F_{vib}(a,T) = \sum_{j\mathbf{q}} \left[\frac{1}{2}\hbar\omega_{j\mathbf{q}}(a) + k_B T \log\left(1 - \exp(-\hbar\omega_{j\mathbf{q}}(a)/k_B T\right) \right]$. In the expression, *a* is the lattice parameter and $\hbar\omega_{j\mathbf{q}}$ is the energy of a phonon in the mode with wave vector, **q**, and polarization, *j*. The first term in brackets gives the contribution from the zero-point motion of the B and P atoms, while the second gives the added contribution from the thermal motion. In the QHA, phonon frequencies are taken to depend explicitly on the lattice parameter. Minimization of F_{QHA} at each temperature gives $a(T)$. Harmonic and anharmonic interatomic force constants (IFCs) are then calculated at each $a(T)$ to obtain phonon modes, three-phonon scattering rates and thermal conductivity at each temperature.

The zero-point motion in BP is large because of the light atoms, increasing the BP lattice constant by 0.3%. For the calculations performed here using the LDA exchange-correlation functional, the QHA gives excellent agreement between the calculated and measured LO phonon frequency at Γ. In BP, the scattering of heat-carrying acoustic phonons by optic phonons is particularly important. Specifically, scattering between two acoustic (*a*) phonons and one optic (*o*) phonon (*aao* processes) dominates the intrinsic thermal resistance. Lowering the optic phonon branches increases the *aao* scattering rates with corresponding reduction in thermal conductivity. The increased lattice parameter from including F_{vib} in F_{QHA} lowers slightly the optic phonon frequencies, which reduces the calculated thermal conductivity values giving better agreement with both the magnitudes and the temperature dependence of the measured data, particularly in the 300K-600K range.

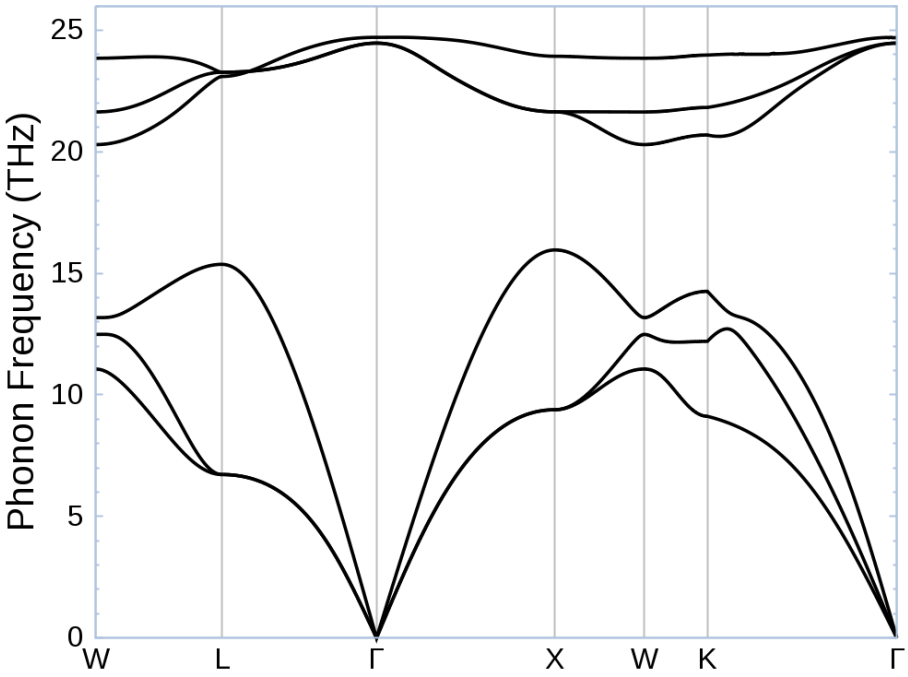

Figure S2. Phonon dispersions of BP along high symmetry directions calculated from first principles in the quasi-harmonic approximation at 300K.

Discussion about TDTR thermal penetration depth and the interfaces involving silver paint

The interface thermal conductance between sample and sample and silver paste and sample and copper foil do not matter for our TDTR measurements. The thermal penetration depth in the sample is $d_p = \sqrt{\Lambda / (Cf\pi)}$, where Λ is thermal conductivity, C is the volumetric heat capacity, f is the modulation frequency.[2] In our study of BP and ^{11}BP, the largest d_p occurs at the lowest temperature (120 K) when the Λ reaches a maximum and C reaches a minimum in our measurement. Taking the value for ^{11}BP, Λ = 1700 W m^{-1} K^{-1}, C = 0.64 J m^{-3} K^{-1}, with f = 1.1 MHz, d_p = 30 μm and at least one order of magnitude smaller than the typical sample thickness (>200 μm) based on SEM observation. Therefore, we do not detect the interface between the BP sample and the Cu foil in our TDTR measurements.

Results of interface thermal conductance

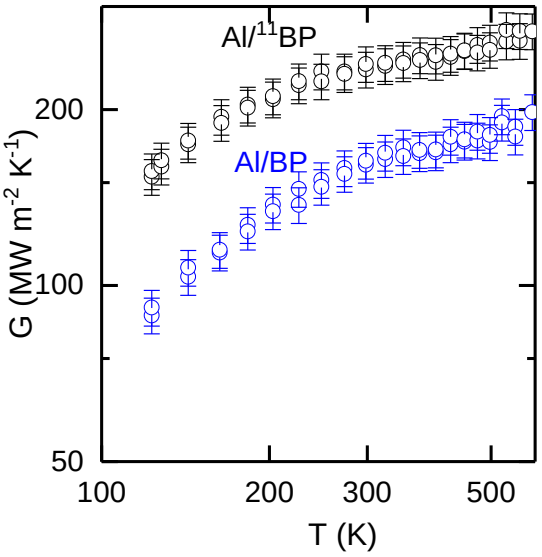

Figure S3. Representative thermal conductance at Al/BP and Al/^{11}BP interfaces as a function of temperature from 120 to 600 K measured by TDTR.

The thermal conductance of the interface between Al transducer and BP and ^{11}BP samples that we measured in the main text are shown in Figure S3. The room temperature values are approximately 180 MW m^{-2} K^{-1} and 220 MW m^{-2} K^{-1}, for Al/BP and Al/^{11}BP respectively. Among samples grown from the same batch we measured, the room temperature interface thermal conductance varies by around 20% for both Al/BP (from 150 to 190 MW m^{-2} K^{-1}) and Al/^{11}BP (from 170 in 220 MW m^{-2} K^{-1}) presumably due to the variation of the surface oxide thickness. Such values are commonly observed for a clean metal/dielectric crystal interface, e.g. ≈200 MW m^{-2} K^{-1} for Al/Si, ≈200 MW m^{-2} K^{-1} for Al/GaN, ≈180 MW m^{-2} K^{-1} for Al/Al_2O_3.[3] The thermal conductivity of these samples measured with w_0 = 10.4 μm also shows around 20% variation with values between 390 to 480 W m^{-1} K^{-1} in BP and 440 to 530 W m^{-1} K^{-1} in ^{11}BP presumably due to the variation of the defect density.

Discussion about the Raman spectra

The shift of the LO(Γ) phonon peak in ^{11}BP from BP is mainly from the change of the average atomic mass. In the harmonic approximation, the optical zone center phonon frequencies of zinc blende compounds are proportional to the inverse square root of the reduced mass, *i.e.* $\omega \propto 1/\sqrt{\mu}$ where $\mu^{-1} = m_{cation}{}^{-1} + m_{anion}{}^{-1}$. The ratio of the first order LO(Γ) phonon frequency, $\omega_{LO(\Gamma)}(BP)/\omega_{LO(\Gamma)}(^{11}BP) \approx 1.0085$ we obtained, is comparable to the ratio $\sqrt{\mu(^{11}BP)}/\sqrt{\mu(BP)} \approx 1.0071$.[4] The deviation may result from a small change of the lattice constant and interatomic force.[5]

In polar semiconductors the plasmons of free carriers interact with the LO phonons via Long-range Coulomb interactions when the plasmon frequency is close to the LO phonon frequency resulting in two coupled LO phonon–plasmon (LPP) modes that are both shifted from the LO phonon frequency in the absence of free carriers.[6] Due to the lack of knowledge about the carrier concentration and effective mass in BP, we were not able to calculate the LPP mode shift in our samples. In a previous literature study of BP and ^{10}BP thin film, grown by chemical vapor deposition (CVD), with n-type carrier concentration of 3.7 ×10^{17} cm^{-3} and 7.5 ×10^{17} cm^{-3}, respectively, an extra peak appears in BP next to the LO peak, similar to what our Raman spectrum, but is not observed in ^{10}BP with higher carrier concentration.[5] If the LPP is the cause of the extra peak in BP, two peaks with even larger splitting should be expected in ^{10}BP. The absence of an extra peak in the ^{10}BP thin film is contradictory to this hypothesis. In addition, the LPP coupling generally leads to a broadening of the LO peak resulting in a FWHM on the order of tens of cm^{-1} when the carrier concentration is high. In contrast, the LO peak FWHM of both BP and ^{11}BP in our measurement is about 7 cm^{-1}. Therefore, we believe the extra 797 cm^{-1} peak in BP does not results from LPP.

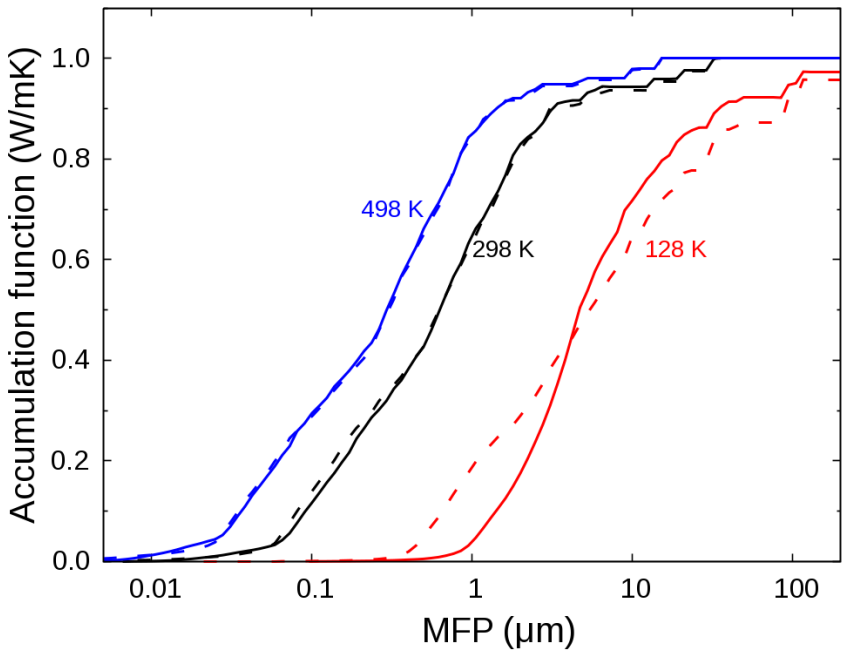

Figure S4. Accumulation functions vs. phonon mean free path (MFP) for ^{11}BP (solid lines) and BP (dash lines) at 128 K, 298 K, 498 K from first-principles calculations. The function is defined in Ref [7].

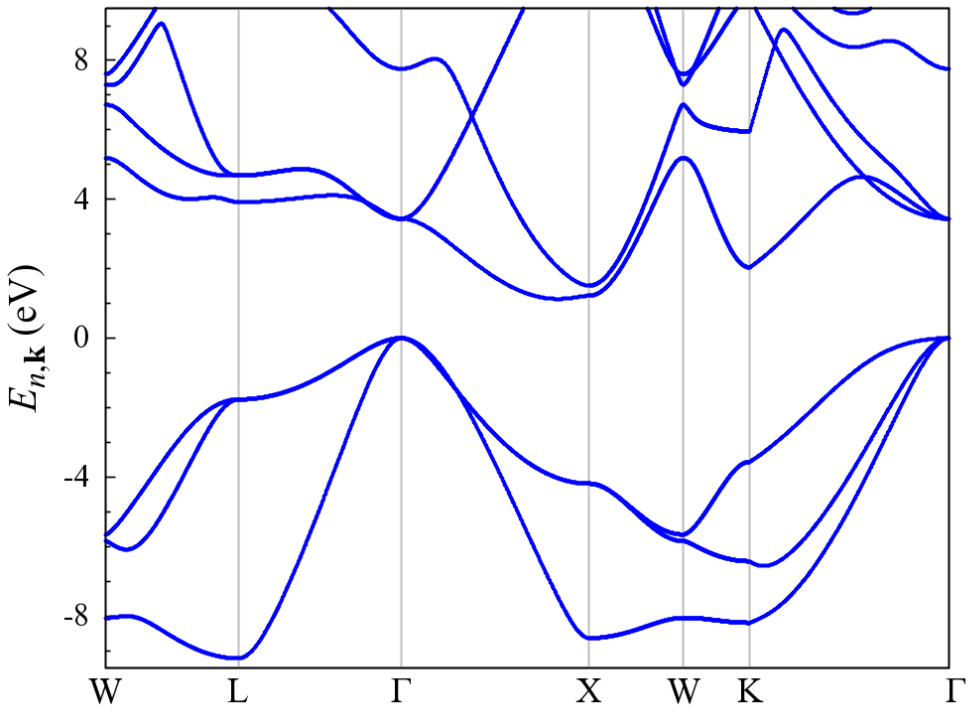

Figure S5. Electronic band structure of BP obtained from our DFT calculation.

Electronic band structure of BP

The electronic structure of BP calculated using density functional theory (DFT) using local density approximation (LDA) of the exchange correlation functional (See Figure S5.) is in good agreement with that calculated previously.[4] The DFT calculations show that BP is a semiconductor, consistent with the other boron-based III-V compounds (BN, BAs, and BSb) with indirect gap of about 1.1 eV. The energy gap is about half of the measured value of 2 eV,[5] which is typical for the error in energy gaps calculated using DFT. The Intrinsic carrier densities in such a semiconductor will be extremely small and not interfere with heat management. The typical electrical resistivity of BP with carrier concentration of $\approx 10^{15}$ cm^{-3} is > 10^2 Ω cm.[10] The lowest resistivity value reported is 0.15 Ω cm in n-type doped BP with carrier concentration of 3.7×10^{17} cm^{-3}.[6] A low electrical conductivity may provide advantage of low losses for heat spreader in high frequency rf electronics.

[1] Y. Kumashiro, T. Mitsuhashi, S. Okaya, F. Muta, T. Koshiro, Y. Takahashi, M. Mirabayashi, Journal of Applied Physics 1989, 65, 2147; J. Ohsawa, T. Nishinaga, S. Uchiyama, Japanese Journal of Applied Physics 1978, 17, 1059.
[2] Y. K. Koh, S. L. Singer, W. Kim, J. M. Zide, H. Lu, D. G. Cahill, A. Majumdar, A. C. Gossard, Journal of Applied Physics 2009, 105, 054303.
[3] R. Stoner, H. Maris, Physical Review B 1993, 48, 16373; H.-K. Lyeo, D. G. Cahill, Physical Review B 2006, 73, 144301; R. Cheaito, J. T. Gaskins, M. E. Caplan, B. F. Donovan, B. M. Foley, A. Giri, J. C. Duda, C. J. Szwejkowski, C. Constantin, H. J. Brown-Shaklee, Physical Review B 2015, 91, 035432.
[4] J. Zhang, T. Ruf, M. Cardona, O. Ambacher, M. Stutzmann, J.-M. Wagner, F. Bechstedt, Physical Review B 1997, 56, 14399; A. Göbel, T. Ruf, C.-T. Lin, M. Cardona, J.-C. Merle, M. Joucla, Physical Review B 1997, 56, 210.
[5] Y. Kumashiro, Y. Okada, H. Okumura, Journal of Crystal Growth 1993, 132, 611.
[6] G. Irmer, M. Wenzel, J. Monecke, Physical Review B 1997, 56, 9524; A. Mooradian, G. Wright, Physical Review Letters 1966, 16, 999; T. Kozawa, T. Kachi, H. Kano, Y. Taga, M. Hashimoto, N. Koide, K. Manabe, Journal of applied physics 1994, 75, 1098.
[7] D. A. Broido, Lucas Lindsay and T. L. Reinecke, Physical Review B 2013, 88, 214303..
[8] S. Bağci, S. Duman, H. Tütüncü, G. Srivastava, Physical Review B 2009, 79, 125326.
[9] V. Fomichev, I. Zhukova, I. Polushina, Journal of Physics and Chemistry of Solids 1968, 29, 1025.
[10] Y. Kumashiro, Journal of Materials Research 1990, 5, 2933.